Front. Phys. 12(4), 126501 (2017)
DOI 10.1007/s11467-016-0614-1

RESEARCH ARTICLE

Spin-resolved quantum transport in graphene-based nanojunctions

Jian-Wei Li[1], Bin Wang[1,*], Yun-Jin Yu[1], Ya-Dong Wei[1], Zhi-Zhou Yu[2], Yin Wang[2,†]

[1] *College of Physics and Energy, Shenzhen University, Shenzhen 518060, China*
[2] *Department of Physics, The University of Hong Kong, Hong Kong, China*
*Corresponding authors. E-mail: *binwang@szu.edu.cn, †yinwang@hku.hk*
Received July 20, 2016; accepted August 4, 2016

First-principles calculations were performed to explore the spin-resolved electronic and thermoelectric transport properties of a series of graphene-nanoribbon-based nanojunctions. By flipping the magnetic moments in graphene leads from parallel to antiparallel, very large tunneling magnetoresistance can be obtained under different gate voltages for all the structures. Spin-resolved alternating-current conductance increases versus frequency for the short nanojunctions but decreases for the long nanojunctions. With increasing junction length, the behavior of the junctions changes from capacitive-like to inductive-like. Because of the opposite signs of spin-up thermopower and spin-down thermopower near the Fermi level, pure spin currents can be obtained and large figures of merit can be achieved by adjusting the gate voltage and chemical potential for all the nanojunctions.

Keywords TMR, AC conductance, thermoelectric transport, NEGF-DFT

PACS numbers 65.80.-g, 72.15.Jf, 72.25.Hg

1 Introduction

The idea of using single molecules as basic functional units for electronic device operation dates back to 1974 when Aviram and Ratner discussed the working principle of a molecular rectifier [1]. Since then, there have been numerous theoretical and experimental investigations on charge and spin transport through various molecular junctions [2–8]. However, there is a significant shortcoming of molecular junctions: Electric conduction is too sensitive to the connection between the molecule and leads, leading to uncertainty of quantum transport properties in molecular junctions. Although one may carefully control the connecting details in a research laboratory, it would be extremely hard — if not outright impossible — to reach such a high degree of control in large-scale practical fabrication. Graphene is one of the most exciting low-dimensional materials owing to its extraordinary properties and is widely studied in materials science and condensed matter physics research, having received extensive attention as its fabrication in 2004 [9]. Good conductivity and high mobility of charge carriers herald broad prospects for graphene in nanoscale electronic device manipulation. Recently, graphene-based all-carbon nanoscale electronic devices have been realized experimentally with the rapid development of precision cutting techniques, e.g., helium ion beam etching [10] and thermally activated nickel nanoparticle etching [11]. Compared with other molecular junctions, graphene-based all-carbon nanojunctions are much more stable and mechanically flexible because the nanocontact rests on the stable C–C chemical bonds. Numerous investigations have been conducted to investigate quantum transport in such all-carbon nanojunctions [12–18].

Quantum transport under dynamic conditions is one of the fundamental research areas in condensed matter physics [19, 20]. Recently, the dynamic responses of nanoscale electronic devices under a high-frequency external bias have been experimentally detected [21–24]. Besides the time-dependent behaviors of the transient current [25–29], another important problem of dynamic investigation is the response of alternating current (AC) conductance to the external frequency. When an AC bias is applied to a system, the current in the system consists of two parts: the particle current and the displacement current. The former describes the in-

*Recent Progress on Quantum Transport in Nano and Mesoscopic Systems (Eds. Qing-Feng Sun, Zhen-Hua Qiao & Xin-Qi Li).

jected current from the leads resulting from the external bias, and the latter comes from the induced charge as a result of Coulomb interaction. As a result, both particle current and displacement current contribute to AC conductance to maintain charge conservation and gauge invariance [30]. Theoretical methods based on scattering matrix theory (SMT) [31, 32] and the nonequilibrium Green's function (NEGF) [30, 33, 34] have been proposed to investigate AC transport from phenomenological theory to precise formulas. By combining NEGF with density functional theory (DFT), first-principles calculation has been performed to investigate AC transport in nanojunctions and tremendous efforts have been devoted to this subject [35–41].

The thermoelectric effect in nanoscale structures has attracted considerable attention in recent years [42–44]. Exploiting the effect is considered to be a feasible solution to solving the heat-generating problem in nanoscale devices by transferring the dissipating heat to electric energy directly. Recently, a new research area focused on the spin Seebeck effect, in which magnons and phonons are believed to play crucial roles, has offered the potential to manipulate the spin by heat and induce spin voltage by using a temperature difference [45–48]. Research on the spin Seebeck effect greatly promotes the development of thermoelectronics and spintronics in further nanoscale device fabrication and application. Thermoelectric transport in nanoscale systems is also interesting because it can provide more information than electronic transport. For instance, the sign of thermopower demonstrates the current direction in the device at low temperature. Numerous investigations have been conducted both theoretically and experimentally to investigate theremoelectric transport properties in graphene-based nanojunctions [49–53]. Previous investigation indicated that the sign of thermopower in a monolayer graphene system is reversed with the change of majority carriers from electrons to holes by the electron–hole asymmetry [51, 52]. Experimental investigation has demonstrated that thermopower shows roughly a linear behavior versus temperature at low temperature, which indicates that phonon-induced thermal conductance can be ignored in graphene [51]. For two-probe systems with zigzag graphene nanoribbon (ZGNR) leads, very large thermal magnetoresistance (TMR) from 10^4 to 10^5 can be obtained when the system is changed from ferromagnetic (FM) to antiferromagnetic (AFM) states [52, 53].

In this paper, first-principles calculations based on the NEGF-DFT method [54] were performed to explore the quantum transport properties of several graphene-based all-carbon nanojunctions. By calculating the transmission coefficients, AC conductances, and thermopowers, several interesting pieces of information were obtained. First, a very large TMR can be obtained for all the structures under different gate voltages. Second, with increasing junction length, the behavior of the structures changes from capacitive-like to inductive-like. Third, a pure spin-resolved current and a pure spin current can be achieved by adjusting the gate voltage. Finally, a large figure of merit can be achieved by adjusting the chemical potential and the gate voltage. Numerical results indicate that ZGNR-polyacene-ZGNR nanojunctions are good candidates for spintronic and thermoelectronic devices.

The rest of this paper is organized as follows. In Section 2, the NEGF-DFT formalism for calculating spin-resolved electronic and thermoelectric transport properties is introduced. In Section 3, the numerical results of spin-resolved transmission, AC conductance, emittance, and spin-resolved thermopower are presented for both FM and AFM configurations of graphene-based nanojunctions. Finally, a summary is given in Section 4.

2 Numerical method and theoretical formulas

In this section, we first show the schematic structure of a graphene-based nanojunction and outline the numerical methods. Then we briefly introduce the theoretical formulas of direct current (DC) transport, AC transport, and thermal transport in magnetic systems.

Figure 1 shows the schematic structure of a graphene-based nanojunction, in which two hydrogenated ZGNR leads of width $N_z = 4$ are joined by a polyacene molecule of length $N = 5$ (where N is the number of rings). Polyacene molecules can be considered as the minimum units of graphene; they connect the two ZGNR leads by C–C bonds seamlessly through removing a pair of hydrogen atoms at both ends. In our calculation, the magnetic moments on both edges of the ZGNR leads are set par-

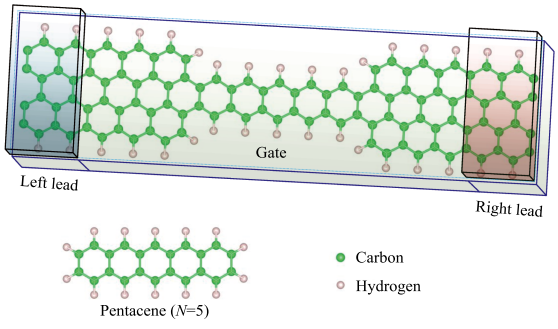

Fig. 1 Schematic of ZGNR-polyacene-ZGNR junction consist of a pentacene molecule connected by two semi-infinite ZGNRs with width $M = 4$. Blue and red bulks at left and right indicate the lead regions where a bias or temperature difference are applied. Gate voltage is applied in the central region. Pentacene molecule with number of carbon rings N=5 is illustrated in the lower panel.

allel, because the antiparallel configurations of ZGNRs exhibit semiconducting behavior. Structure relaxation and transport calculations were performed using Nanodcal, which is based on the standard NEGF-DFT method [54]. An ultra-soft pseudopotential was used to define the core [55] and an single-ζ polarized(SZP) basis set was adopted to describe the valence electron. The exchange correlation was treated at the local spin density approximation(LSDA) level [56] and the real-space cutoff energy was set to 400 Ry. All the atoms are restricted on the plane to relax the total energy until the force exerted on each atom is <0.05 eV/Å. In quantum transport investigation, a self-consistent Hamiltonian was obtained until its average numerical tolerance became $<10^{-4}$ eV.

Once the Hamiltonian is obtained, one can construct the nonequilibrium Green's function to describe quantum transport in the system. Under a DC condition, the spin-resolved electric current I_σ can be calculated using Landauer–Büttiker formula as follows (in which $q = 1$ and $h = 2\pi$) [57]:

$$I_\sigma = -\frac{q}{h}\int \mathcal{T}_\sigma(E)(f_L - f_R)\mathrm{d}E, \tag{1}$$

where the subscript $\sigma = \uparrow, \downarrow$ indicates the spin index. f_L and f_R are the Fermi distribution functions of lead L and lead R, respectively. $\mathcal{T}_\sigma$ is the nonequilibrium spin-resolved transmission coefficient, which can be calculated by

$$\mathcal{T}_\sigma = \mathrm{Tr}[\Gamma_L G^r \Gamma_R G^a]_{\sigma\sigma}, \tag{2}$$

where G^r and G^a are the retarded and advanced Green's function, respectively, and Γ_L and Γ_R are the linewidth functions that describe the coupling between the leads and the scattering region. In the equilibrium state, the spin-resolved DC conductance G_σ is equal to $e^2/h\mathcal{T}_\sigma(E_F)$, where E_F is the Fermi level.

When an AC bias is applied between the two leads, both particle current and displacement current contribute to the AC conductance. If the AC bias is cosinoidal, i.e., $v_\alpha(t) = v_\alpha \cos(\omega t)$, the spin-resolved AC conductance as a function of the external frequency can be evaluated by [26]

$$G_{\alpha\beta,\sigma}(\omega) = G^c_{\alpha\beta,\sigma}(\omega) - G^d_{\beta,\sigma}(\omega)\frac{\sum_\gamma G^c_{\alpha\gamma,\sigma}(\omega)}{\sum_\gamma G^d_{\gamma,\sigma}(\omega)}, \tag{3}$$

where the subscripts $\alpha, \beta, \gamma = L, R$ indicate the left and right leads. $G^c_{\alpha\beta,\sigma}$ denotes the conductance contributed by the particle current and $G^d_{\beta,\sigma}$ comes from the displacement current. The detailed expressions for $G^c_{\alpha\beta,\sigma}$ and $G^d_{\beta,\sigma}$ can be found in Ref. [30].

For a low-frequency external bias, $G_{\alpha\beta,\sigma}(\omega)$ can be expanded as a function of ω as follows:

$$G_{\alpha\beta,\sigma}(\omega) = G_{\alpha\beta,\sigma}(0) - \mathrm{i}\omega E_{\alpha\beta,\sigma} + \omega^2 K_{\alpha\beta,\sigma} + O(\omega^3) + \cdots, \tag{4}$$

where $G_{\alpha\beta,\sigma}(0)$ is the spin-resolved DC conductance with $G_{LL,\sigma}(0) = -G_{LR,\sigma}(0) \equiv G_\sigma$; $E_{\alpha\beta,\sigma}$ is the spin-resolved emittance, which describes the phase difference between the current and voltage at low frequency; and $K_{\alpha\beta,\sigma}$ is the dynamic dissipation at low frequency, which shows the high-order response to AC conductance.

To investigate spin-resolved thermoelectric transport properties, a temperature gradient ΔT and a bias voltage ΔV should be applied simultaneously between the two leads. The spin-resolved thermopower S_σ measures the ΔV needed to neutralize the spin-resolved electric current I_σ caused by ΔT. When $I_\sigma = 0$, a spin-polarized heat current I^Q_σ exists in the system that flows from the lead at high temperature to the lead at low temperature. The thermal conductance κ_σ is defined as $I^Q_\sigma/\Delta T$. In the limit of a small bias voltage and a low temperature gradient, S_σ and κ_σ can be expressed as [58]

$$S_\sigma(\mu, T) = -\frac{1}{eT}\frac{K_{\sigma,1}(\mu, T)}{K_{\sigma,0}(\mu, T)} \tag{5}$$

and

$$\kappa_\sigma(\mu, T) = \frac{1}{hT}\left[K_{\sigma,2}(\mu, T) - \frac{K^2_{\sigma,1}(\mu, T)}{K_{\sigma,0}(\mu, T)}\right], \tag{6}$$

where $K_{\sigma,n}(\mu, T)$ is defined as

$$K_{\sigma,n}(\mu, T) = -\int_{-\infty}^{+\infty}(\epsilon - \mu)^n \frac{\partial f(\epsilon, \mu, T)}{\partial E}\mathcal{T}_\sigma(\epsilon)\mathrm{d}\epsilon. \tag{7}$$

The figure of merit describes the thermoelectric conversion performance of a nonmagnetic material. For a magnetic system, the concept is generalized to spin figure of merit, which describes the conversion efficiency from heat to spin voltage. The charge and spin figures of merit are defined as [49, 50]

$$ZT_{ch(sp)} = \frac{S^2_{ch(sp)} G_{ch(sp)} T}{\kappa}, \tag{8}$$

where S_{ch} and S_{sp} are charge and spin thermopower, respectively, and are defined as $S_{ch} = (S_\uparrow + S_\downarrow)/2$ and $S_{sp} = S_\uparrow - S_\downarrow$; $G_{ch} = G_\uparrow + G_\downarrow$, $G_{sp} = |G_\uparrow - G_\downarrow|$; and $\kappa = \kappa_\uparrow + \kappa_\downarrow$. Note that the κ in Eq. (8) includes only the contribution from electrons in our calculation and the effect of phonons is not considered. This is reasonable for graphene systems at low temperature ($T < 100$ K) as indicated in Ref. [49].

3 Results and discussion

In this section, we show the numerical results and give a physical understanding to the quantum transport properties of a series of ZGNR-polyacene-ZGNR structures

including the transmission coefficient, TMR, dynamic conductance, emittance, thermopower, and figure of merit.

3.1 DC transport properties

We first investigate the DC transport properties for the FM configuration of a ZGNR-polyacene-ZGNR nanojunction as shown in Fig. 1, where the net magnetic moments in both leads are parallel. Figure 2(a) and Fig. 2(b) show the spin-resolved transmission coefficients $\mathcal{T}_\uparrow$ and $\mathcal{T}_\downarrow$ as functions of energy E, respectively, for nanojunctions with $N = 5, 6, 7$, and 8. Two main features can be discerned in the two panels. (i) Both $\mathcal{T}_\uparrow$ and $\mathcal{T}_\downarrow$ show several peaks for each different N. With N increasing from 5 to 8, the broad peaks of $\mathcal{T}_\uparrow$ shrink toward the sharp peak at $E_0 \approx -0.22$ eV, while the broad peaks of $\mathcal{T}_\downarrow$ move toward a specific energy $E_0 \approx 0.28$ eV where $\mathcal{T}_\downarrow$ increases rapidly. The behaviors of $\mathcal{T}_\sigma$ near E_0 are barely changed with increasing N. Because the spin-resolved edge states of ZGNR appear at E_0, we conclude that the sharp peaks of $\mathcal{T}_\uparrow$ and the rapid increase of $\mathcal{T}_\downarrow$ near E_0 are dominated by the spin-resolved edge states of ZGNR leads. (ii) With N increasing from 5 to 8, $\mathcal{T}_\uparrow(E_F)$ increases with a positive gradient, and $\mathcal{T}_\downarrow(E_F)$ increases with a negative gradient. To understand this behavior, we calculated the renormalized molecular levels (RMLs) of *isolated* polyacene molecule with different N values and plotted the lowest unoccupied molecular orbital (LUMO) levels of spin-up states in Fig. 2(a) and the highest occupied molecular orbital (HOMO) levels of spin-down states in Fig. 2(b). Obviously, the LUMO state above the Fermi level contributes most to $\mathcal{T}_\uparrow(E_F)$, so its gradient is positive, whereas the HOMO state below the Fermi level contributes most to $\mathcal{T}_\downarrow(E_F)$, so its gradient is negative. In addition, the spin-up LUMO level and spin-down HOMO level approach the Fermi level gradually with increasing of N; therefore $\mathcal{T}_\uparrow(E_F)$ and $\mathcal{T}_\downarrow(E_F)$ increase versus N.

Figure 2(c) and Fig. 2(d) show $\mathcal{T}_\uparrow$ and $\mathcal{T}_\downarrow$, respectively, as functions of energy E for the FM configuration of a nanojunction with $N = 6$ under different gate voltages. In our calculation, the gate voltage is applied in the molecular region along the direction perpendicular to the system plane. To realize this point, an initial uniform electric field is applied in the molecular region perpendicular to the ZGNR plane to model the gate voltage. The final effective potential is determined self-consistently from first-principles calculation. With increasing gate voltage, the spin-up LUMO level is pushed close to the

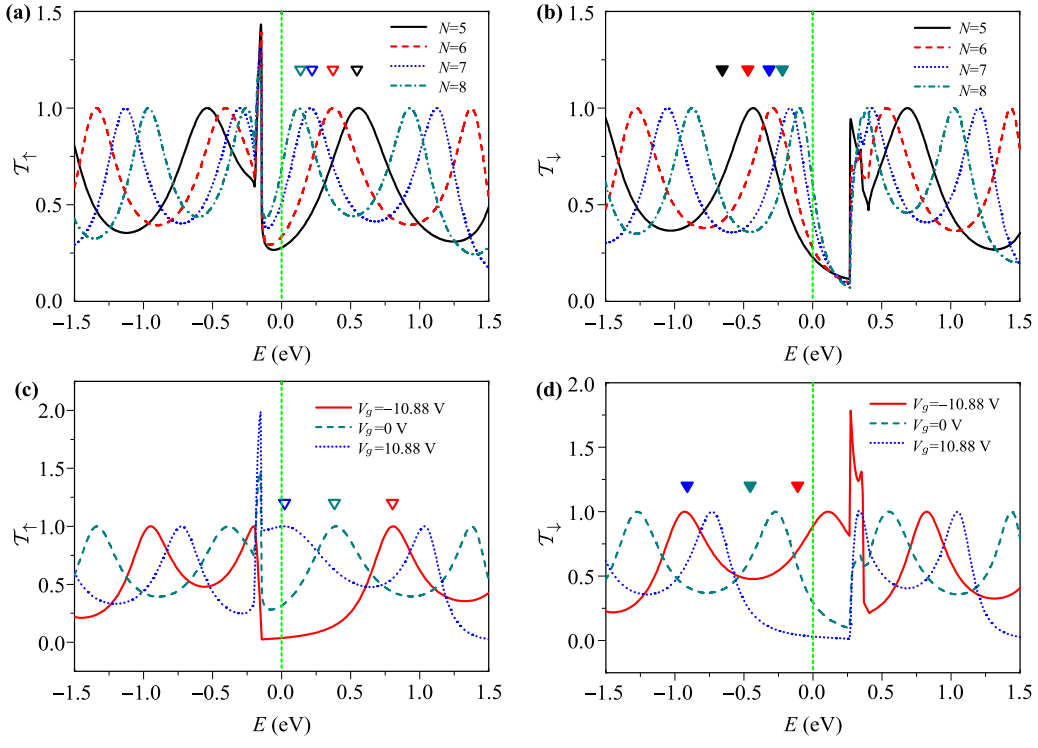

Fig. 2 $\mathcal{T}_\sigma$ as a function of E for the FM configurations of ZGNR-polyacene-ZGNR molecular junctions. **(a)** $\mathcal{T}_\uparrow$ and **(b)** $\mathcal{T}_\downarrow$ for the junctions with different N. **(c)** $\mathcal{T}_\uparrow$ and **(d)** $\mathcal{T}_\downarrow$ for the junction with $N = 6$ under different V_g. In panel (a) and (c), the open downward triangles indicate the renormalized LUMO levels for different N and different V_g, respectively. In panel (b) and (d), the solid downward triangles indicate the renormalized HOMO levels for different N and different V_g, respectively.

Fermi level and the spin-down HOMO level is pushed far away from the Fermi level. Therefore, $\mathcal{T}_\uparrow(E_F)$ increases and $\mathcal{T}_\downarrow(E_F)$ decreases as functions of gate voltage.

To further evaluate the efficiency of gate voltage in regulating quantum transport, we calculated the gap between the renormalized LUMO state and the HOMO state of an *isolated* polyacene molecule by changing the gate voltage. Furthermore, we projected the scattering state at the Fermi level to LUMO and HOMO to quantify the contribution of RMLs to the transmission coefficient of the system. Figure 3(a) shows plots of E_σ(LUMO) and E_σ(HOMO) as functions of gate voltage from −10 to 10 V for a ZGNR-polyacene-ZGNR nanojunction with $N = 6$. Both E_σ(LUMO) and E_σ(HOMO) show roughly linearly behavior for both spin-up and spin-down channels. The linear fitting of RMLs versus gate voltage indicates that the slope is ∼0.036 eV/V, which means that the efficiency of the gate voltage is ∼3.6%. Obviously, although the gate voltage seems large in our calculation, the gating efficiency to the device is quite low because the plane of the atomic device is perpendicular to the gate voltage.

Figure 3(b) shows the projection of scattering states at $E = E_F$ to RMLs, where the projection coefficient P_σ is defined as

$$P_\sigma(\mathrm{RML}) = |\langle\phi_\sigma(\mathrm{RML})|\Psi_\sigma(E_F)\rangle|^2. \tag{9}$$

Here, ϕ_σ(RML) is the spin-resolved eigenstate of an *isolated* molecule at LUMO and HOMO, and $\Psi_\sigma(E_F)$ is the spin-resolved scattering state at the Fermi level of the device. P_σ describes the contribution of renormalized molecular states to the transmission coefficient at the Fermi level. As shown in Fig. 3(b), $P_\uparrow$(LUMO) increases from 60% to 100% versus gate voltage from −10 to 10 V, which indicates a closing of the spin-up LUMO to the Fermi level, whereas $P_\downarrow$(HOMO) decreases from 100% to 60%, which indicates a movement of the spin-down HOMO away from the Fermi level. In addition, $P_\uparrow$(HOMO) and $P_\downarrow$(LUMO) are always zero under all the gate voltage, which means zero contributions of the spin-up HOMO to $\mathcal{T}_\uparrow(E_F)$ and the spin-down LUMO to $\mathcal{T}_\downarrow(E_F)$. Therefore, we conclude that the conductance G is dominated by $G_\downarrow$ under a negative gate voltage and by $G_\uparrow$ under a positive gate voltage, as shown in Fig. 3(c), where G_σ as a function of gate voltage V_g is given for junctions with different N values. With gate voltage increasing from −10 to 10 V, $G_\uparrow$ increases roughly from zero to one, whereas $G_\downarrow$ decreases roughly from one to zero. As a result, the spin-filtering efficiency η varies from −1 to 1 as a function of V_g, as shown in Fig. 3(d), where η is defined as

$$\eta = \frac{G_\uparrow - G_\downarrow}{G_\uparrow + G_\downarrow}. \tag{10}$$

The very large gate-controlled value of η indicates that the FM configuration of a ZGNR-polyacene-ZGNR nano-

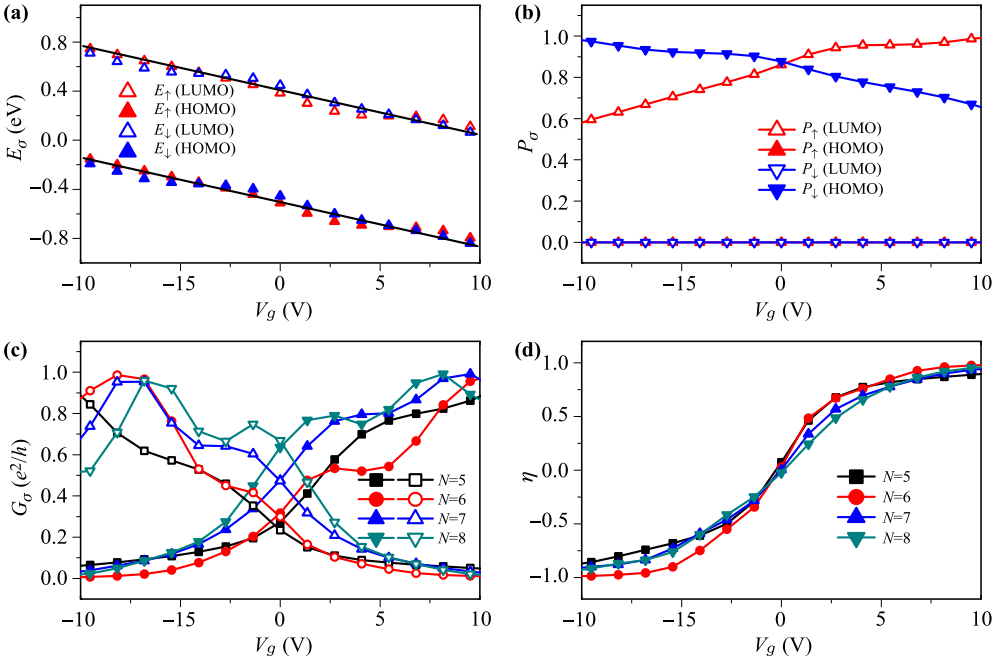

Fig. 3 **(a)** E_σ(LUMO) and E_σ(HOMO), and **(b)** P_σ(LUMO) and P_σ(HOMO) as functions of V_g for FM configuration with $N = 6$. The two lines in (a) are the fitting of LUMOs and HOMOs as functions of V_g with slopes roughly equal to −0.036 eV/V. **(c)** G_σ, and **(d)** η as functions of V_g for the FM configurations with different N. The solid and hollow marker curves in panel (c) indicate the conductance of spin up and spin down electrons, respectively.

junction can work as a perfect spin filter.

In the following, we show DC transport properties for the AFM configuration of a ZGNR-polyacene-ZGNR nanojunction, in which the net magnetic moments in both leads are antiparallel. As a result, the spin-up and spin-down channels in the system are degenerate. Figure 4(a) shows the transmission coefficient of the structures with different N values under zero bias. For each structure, a transmission gap roughly equal to 0.45 eV appears near the Fermi level. It is found that the gap values are not affected by the gate voltage, as shown in Fig. 4(b), although the gate voltage can adjust the transmission peaks, which are dominated by the RMLs, away from the Fermi level. Similar properties have been found in other ZGNR-based nanojunctions [59]. We found that there are two main features that contribute to the gate-independent transmission gap near the Fermi level (1) the AFM configuration of the left and the right ZGNR leads and (2) the symmetric arrangement of polyacene molecule between the two ZGNR leads. As indicated in Ref. [60], transmission coefficients of ZGNR-based nanojunctions depend on the symmetry of transverse wave functions, which expand in the ZGNR plane and are perpendicular to the transport direction. For a ZGNR with a width equal to an even number, the transverse wave function with respect to the centerline of device is an even function for spin-up electrons and an odd function for spin-down electrons. For the FM configuration, the symmetries of transverse wave functions in the left ZGNR lead and the right ZGNR lead are the same, so the transmission coefficients are large for both spin-up and spin-down electrons. However, for the AFM configuration, the symmetries of transverse wave functions in the left and right ZGNR leads are opposite to each other, so a transmission gap appears near the Fermi level. In addition, the connecting formation of the polyacene molecule between the two ZGNR leads is also critical. If the polyacene molecule is not symmetrically connected between the two ZGNR leads in the AFM configuration (e.g., it is put close to one edge of the ZGNR leads), the transmission coefficient near the Fermi level can be greatly increased by adjusting the gate voltage.

The conductance G of the AFM configuration as a function of gate voltage is shown in Fig. 4(c). G exhibits an oscillating behavior versus gate voltage for different N values, although its value stays on the order of $\sim 10^{-4}$ to $\sim 10^{-5}$. As a result, very large TMR (from $\sim 10^{4}$ to $\sim 10^{5}$) can be obtained under different gate voltages, as shown in Fig. 4(d), where TMR is defined as

$$\mathrm{TMR} = \frac{G^{\mathrm{FM}} - G^{\mathrm{AFM}}}{G^{\mathrm{AFM}}}. \tag{11}$$

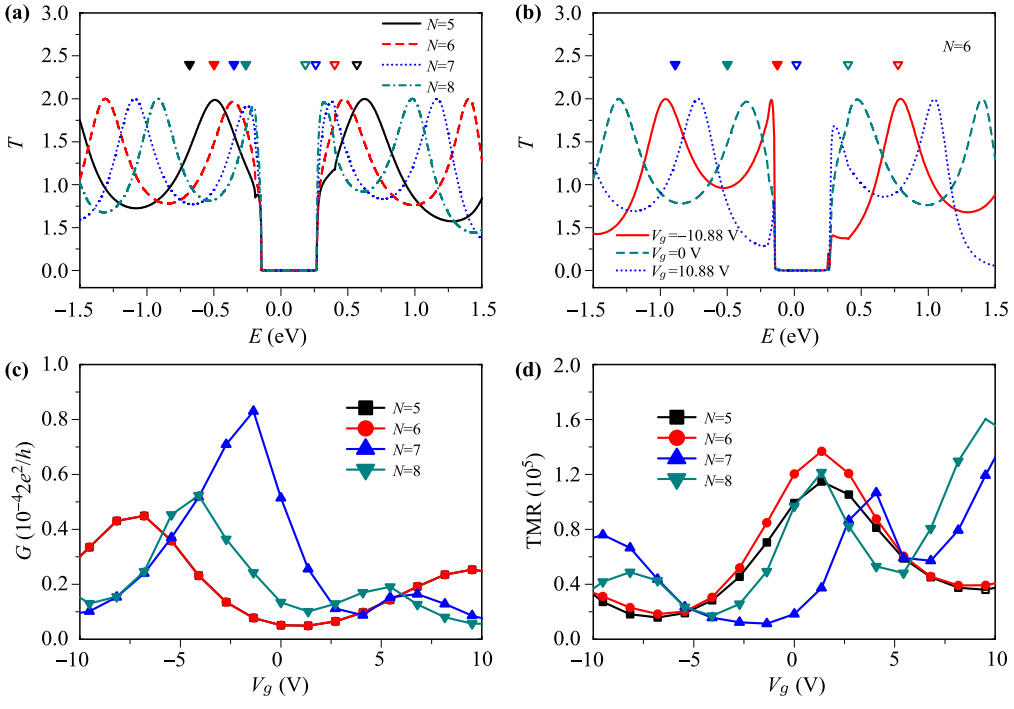

Fig. 4 $\mathcal{T}$ as a function of E for the AFM configurations of **(a)** ZGNR-polyacene-ZGNR molecular junctions with different N and **(b)** ZGNR-polyacene-ZGNR molecular junction with $N = 6$ under different gate voltage. **(c)** G and **(d)** TMR as functions of V_g for the AFM configurations of molecular junctions with different N. In panel (a) and panel (b), the open and solid downward triangles indicate the renormalized LUMO and HOMO levels, respectively.

Here, G^{FM} is the conductance of the FM configuration of the system with $G^{\mathrm{FM}} = G^{\mathrm{FM}}_{\uparrow} + G^{\mathrm{FM}}_{\downarrow}$, and G^{AFM} is the conductance of the AFM configuration of the system. The well-controlled spin-filtering efficiency and very large TMR values indicate that the ZGNR-polyacene-ZGNR junctions are of great significance for device applications in spintronics.

3.2 AC transport properties

In this subsection, we show the numerical results of AC transport properties for FM and AFM configurations of ZGNR-polyacene-ZGNR junctions. Figures 5(a) and (b) present the difference between the real parts of AC conductance $G_{LL,\sigma}(\omega)$ and DC conductance G_σ for spin-up and spin-down electrons of the FM configuration, respectively. The real part of $G_{LL,\sigma}$ is denoted as $G_{\mathrm{R},\sigma}$ in the following. When the frequency ω is equal to zero, $G_{\mathrm{R},\sigma}$ is reduced to the DC conductance G_σ. With increasing ω, $G_{\mathrm{R},\sigma}$ exhibits a nonlinear behavior for both spin-up and spin-down electrons of the structures with different N values. $G_{\mathrm{R},\uparrow}$ is larger than $G_\uparrow$ for $N = 5$ and 6 and smaller than $G_\uparrow$ for $N = 7$ and 8, whereas $G_{\mathrm{R},\downarrow}$ is larger than $G_\downarrow$ for $N = 5, 6$, and 7 and smaller than $G_\downarrow$ for $N = 8$. Figures 5(c) and (d) show the imaginary part of $G_{LL,\sigma}(\omega)$ versus ω for spin-up and spin-down electrons, respectively, which is denoted as $G_{\mathrm{I},\sigma}$ in the following. As a comparison, $-\omega E_{LL,\sigma}$ is also plotted in Figs. 5(c) and (d) by dashed lines. When $\omega < 10$ THz, $G_{\mathrm{I},\sigma}$ is very close to $-\omega E_{LL,\sigma}$ and exhibits roughly linear behavior, whereas, if $\omega > 10$ THz, the magnitude of $G_{\mathrm{I},\sigma}$ becomes smaller than $-\omega E_{LL,\sigma}$ and exhibits nonlinear behavior. According to Eq. (4), we see that, besides G_σ, $G_{\mathrm{R},\sigma}$ is also contributed to by the term $\omega^2 K_{LL,\sigma}$, which determines the sign of $G_{\mathrm{R},\sigma} - G_\sigma$. $G_{\mathrm{I},\sigma}$ is mostly contributed to by $E_{LL,\sigma}$ when ω is small, while the higher order terms of ω become important to $G_{\mathrm{I},\sigma}$ with further increasing ω. For the spin-up channel, $K_{LL,\uparrow}$ and $E_{LL,\uparrow}$ are positive for $N = 5$ and 6, whereas $K_{LL,\uparrow}$ and $E_{LL,\uparrow}$ are negative for $N = 7$ and 8. For the spin-down channel, $K_{LL,\downarrow}$ and $E_{LL,\downarrow}$ are positive for $N = 5, 6$, and 7, whereas $K_{LL,\downarrow}$ and $E_{LL,\downarrow}$ are negative for $N = 8$.

The signs of $E_{\alpha\beta,\sigma}$ and $K_{\alpha\beta,\sigma}$ determine whether the system is capacitive-like or inductive-like in dynamic response. For instance, if $E_{LL,\sigma}$ and $K_{LL,\sigma}$ are positive, the system exhibits capacitive-like behavior for electrons with spin σ, whereas, for negative $E_{LL,\sigma}$ and $K_{LL,\sigma}$, the system behaves inductive-like for electrons with spin σ. This can be qualitatively understood by comparing Eq. (4) to the conductance of classical R-L and R-C circuits. For an R-L circuit,

$$G^{RL}(\omega) = \frac{1}{R} + \mathrm{i}\omega\frac{L}{R^2} - \omega^2\frac{L^2}{R^3}. \tag{12}$$

For an R-C circuit

$$G^{RC}(\omega) = -\mathrm{i}\omega C + \omega^2 C^2 R. \tag{13}$$

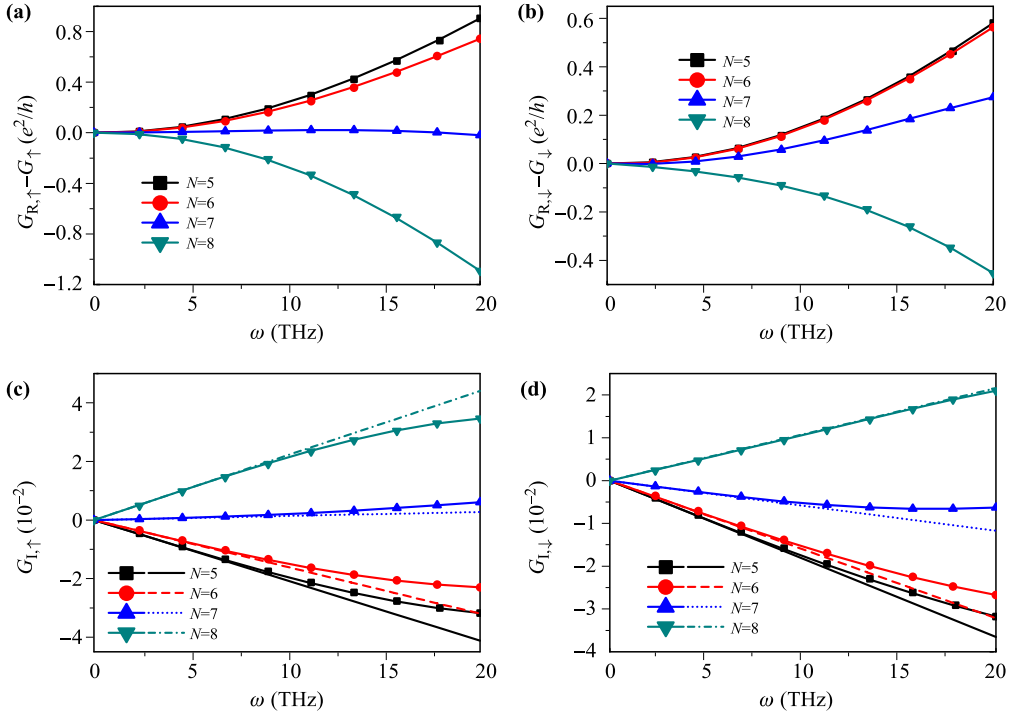

Fig. 5 **(a)** $G_{R,\uparrow}-G_\uparrow$, **(b)** $G_{R,\downarrow}-G_\downarrow$, **(c)** $G_{I,\uparrow}$ and **(d)** $G_{I,\downarrow}$ as functions of ω for the FM configuration of ZGNR-polyacene-ZGNR junctions with $N = 5, 6, 7, 8$. Straight lines in (c) and (d) indicate $-\omega E_{LL}$.

For an R-L circuit, the decreasing conductance and positive imaginary part indicate an inductive behavior, where the voltage lags behind the current, whereas, for an R-C circuit, the positive real part and negative imaginary part of the conductance describe a capacitive behavior, where the current is hysteretic with respect to the voltage.

The sign of $E_{LL,\sigma}$ can be analyzed by further expanding it with the partial density of states $\mathrm{d}n_{\alpha,\sigma}/\mathrm{d}E$. For ZGNR-polyacene-ZGNR nanojunctions, there are only two transmission channels at the Fermi level, and $\mathrm{d}n_{L,\sigma}/\mathrm{d}E = \mathrm{d}n_{R,\sigma}/\mathrm{d}E$ owing to spatial reversion symmetry. In this case, $E_{LL,\sigma}$ can be further reduced to [26, 27]

$$E_{LL,\sigma} = -\frac{1}{4}(2\mathcal{T}_\sigma - 1)\mathrm{Tr}\left[\frac{\mathrm{d}n_\sigma}{\mathrm{d}E}\right]. \quad (14)$$

For structures with $N = 5$ and 6, $\mathcal{T}_\uparrow$ at the Fermi level is <0.5, and thus $E_{LL,\uparrow}$ is positive and the systems exhibit capacitive behavior, whereas, for structures with $N = 7$ and 8, $\mathcal{T}_\uparrow$ at the Fermi level is >0.5, and thus $E_{LL,\uparrow}$ is negative and the system exhibits inductive behavior. A similar analysis for spin-down electrons shows that structures with $N = 5, 6$, and 7 exhibit capacitive-like behavior and a structure with $N = 8$ exhibits inductive-like behavior.

Figures 6(a) and (b) show G_R and G_I versus frequency ω for the AFM configuration of nanojunctions with different N values, respectively. As a comparison, $-\omega E_{LL}$ is also plotted in Fig. 6(b) for all the structures. G_R exhibits nonlinear increasing behavior and G_I is always negative for all the structures, which indicates that the AFM configurations of ZGNR-polyacene-ZGNR nanojunctions always exhibit capacitive-like behaviors for all the structures. This is in accordance with that shown in Fig. 4(a), where $\mathcal{T}(E_F)$ is very close to zero for all the structures. In addition, G_R increases and G_I decreases with N at finite frequency, which indicates an improving capacitive-like behavior for the structures with larger N.

3.3 Thermoelectric transport properties

In this subsection, we investigate the thermoelectric transport behaviors of ZGNR-polyacene-ZGNR nanojunctions. Figures 7(a) and (b) show the spin-resolved thermopower and thermal conductance as functions of temperature at $\mu = 0$ for the FM configurations of nanojunctions with $N = 5, 6, 7$, and 8. S_σ and κ_σ increase linearly with temperature T ranging from 3 to 150 K for all the structures. At a given temperature, S_σ and κ_σ increase with N. In addition, $S_\uparrow$ is always negative, whereas $S_\downarrow$ is always positive. This means that spin-up electrons and spin-down electrons will flow in the opposite direction once a temperature gradient is applied between the two leads of the junction. These properties can be understood by expanding S_σ and κ_σ at low temperature, where $S_\sigma \sim -\frac{T}{G_\sigma}\frac{\partial G_\sigma}{\partial \mu}$ and $\kappa \sim TG_\sigma$. Obviously, both S_σ and κ_σ are linearly proportional to temperature T and the sign of S_σ is determined by $\frac{\partial G_\sigma}{\partial \mu}$. Because $\frac{\partial G_\uparrow}{\partial \mu}|_{\mu=0}$ is positive for all the structures, as shown in Fig. 2(a), $S_\uparrow$ is always negative. In contrast, $\frac{\partial G_\downarrow}{\partial \mu}|_{\mu=0}$ is negative for all the structures, as shown in Fig. 2(b), so $S_\downarrow$ is always positive. The magnitude of S_σ is determined by the competition of G_σ and $\frac{\partial G_\sigma}{\partial \mu}$. Because the growth of $\frac{\partial G_\sigma}{\partial \mu}$ is faster than that of G_σ versus N, the magnitude of S_σ increases as a function of N. κ_σ is proportional to G_σ, so the larger the value of N is, the larger is κ_σ.

By applying a gate voltage in the molecular region, $S_\uparrow$ and $S_\downarrow$ can be adjusted simultaneously. Figure 7(c) shows S_σ versus gate voltage at $T = 20$ K for the FM configuration with $N = 5, 6, 7$, and 8. The magnitude of S_σ can be effectively tuned by the gate voltage. A large positive gate voltage can change the sign of $S_\uparrow$ from neg-

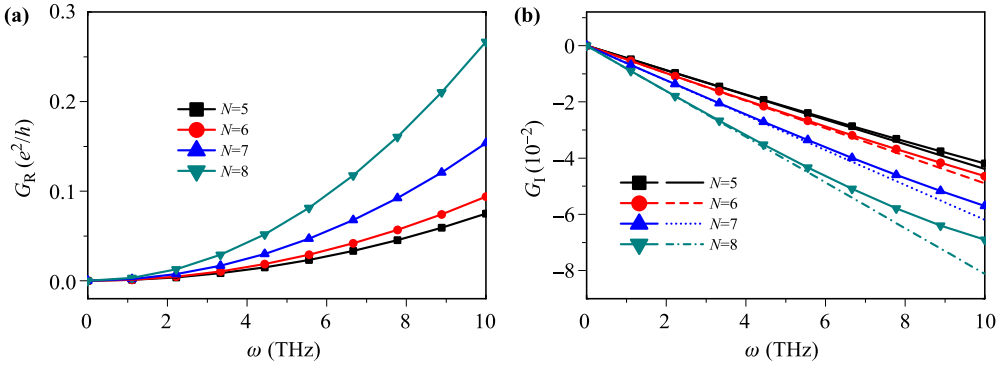

Fig. 6 **(a)** G_R and **(b)** G_I versus ω for the AFM configurations of ZGNR-polyacene-ZGNR junctions with $N = 5, 6, 7, 8$. Straight lines in (b) indicate $-\omega E_{LL}$.

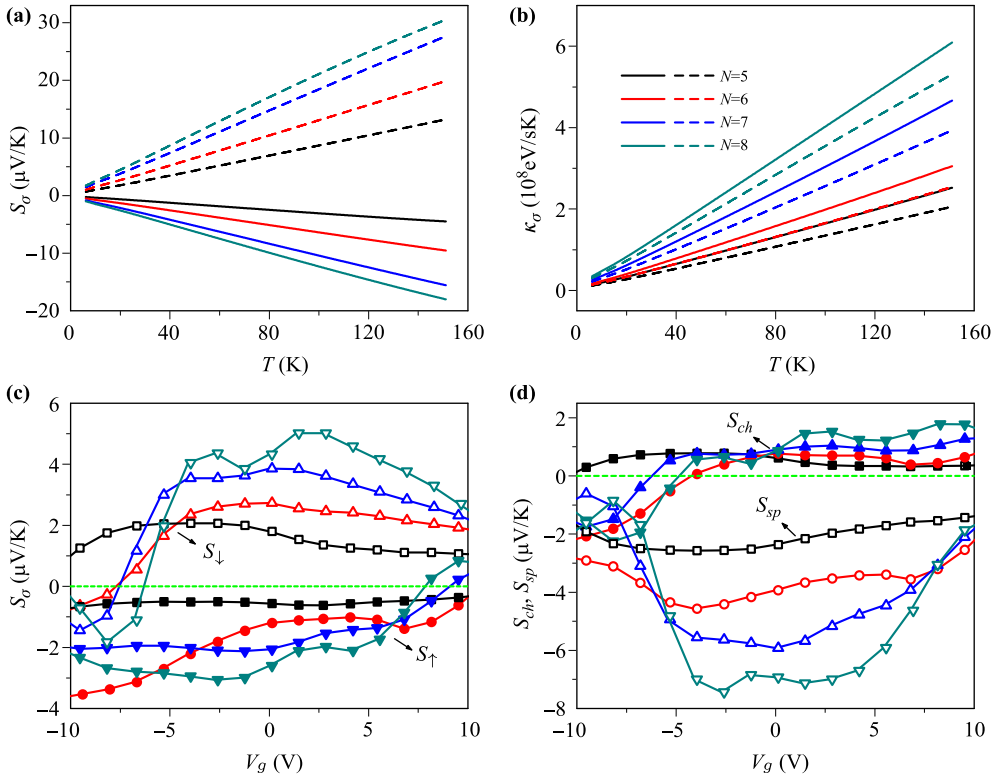

Fig. 7 **(a)** S_σ, **(b)** κ_σ versus temperature for ZGNR-polyacene-ZGNR structures with $N = 5$ (*black curves*), 6 (*red curves*), 7 (*blue curves*), and 8 (*cyan curves*). The solid and dash curve corresponding to spin up and spin down values. **(c)** S_σ, **(d)** $S_{ch,sp}$ versus gate voltage for $N = 5, 6, 7, 8$ at temperature $T = 20$ K. The solid and open symbols correspond to spin up and spin down values, respectively. Different symbols in (c) and (d) indicate different N as shown in Fig. 3.

ative to positive, whereas a large negative gate voltage can change the sign of $S_\downarrow$ from positive to negative. More importantly, pure spin-polarized current and pure spin current can be achieved by tuning the gate voltage. To show this behavior, S_{ch} and S_{sp} versus gate voltage are plotted in Fig. 7(d). Using the structure with $N = 6$ as an example, we see that $S_\downarrow$ vanishes when $V_g \approx -7.6$ V, which indicates that a pure spin-up current occurs in the system because of the temperature gradient. However, at $V_g \approx -4$ V, $S_\uparrow + S_\downarrow = 0$, which means that the left-flowing spin-up current and right-flowing spin-down current are absolutely canceled, so therefore a pure spin current occurs.

Although S_σ can be effectively adjusted by the gate voltage, it is impossible to achieve a large figure of merit at $\mu = 0$ owing to the small S_σ and large G_σ. To achieve a large ZT_{sp}, we scanned the chemical potential μ from -1.5 to 1.5 eV. $S_\uparrow$ and $S_\downarrow$ are small throughout most of the energy range except near E_0, where a rapid change of $\mathcal{T}_\sigma$ appears, as shown in Fig. 2. $\mathcal{T}_\uparrow$ and $\mathcal{T}_\downarrow$ near E_0 are expanded and plotted in Figs. 8(a) and (b), respectively. In these two energy regimes, $S_\uparrow$ and $S_\downarrow$ exhibit very large values accompanied with the quick oscillation as shown in Figs. 8(c) and (d). With gate voltage increasing from -13.61 to 13.61 V, the peak values of $S_\uparrow$ and $S_\downarrow$ decrease from a large positive value to a large negative value with an energy shift. As a result, a very large value of ZT_{sp} can be obtained under various gate voltages, as shown in Figs. 8(e) and (f). As the very large $S_\uparrow$ and $S_\downarrow$ values are located at the hole and electron sides, respectively, ZT_{ch} is very small in comparison with ZT_{sp}. With gate voltage increasing from -13.61 to 13.61 V, the peak of ZT_{sp} decreases on the hole side and increases on the electron side. A large spin figure of merit makes this gate regime more significant for application.

Very large thermopower and figure of merit can also be achieved near the transmission gap for AFM configurations. Figures 9(a) and (b) show the transmission coefficient near the left and right gap edges under different gate voltages. Owing to the abrupt change of transmission coefficient, large thermopower can be obtained as shown in Figs. 9(c) and (d). Gate voltage can adjust the steepness of the transmission slopes near the gap edges and further influences the values of thermopower. Simultaneously, because G is very small in the gap region, large figures of merit are obtained, as shown in

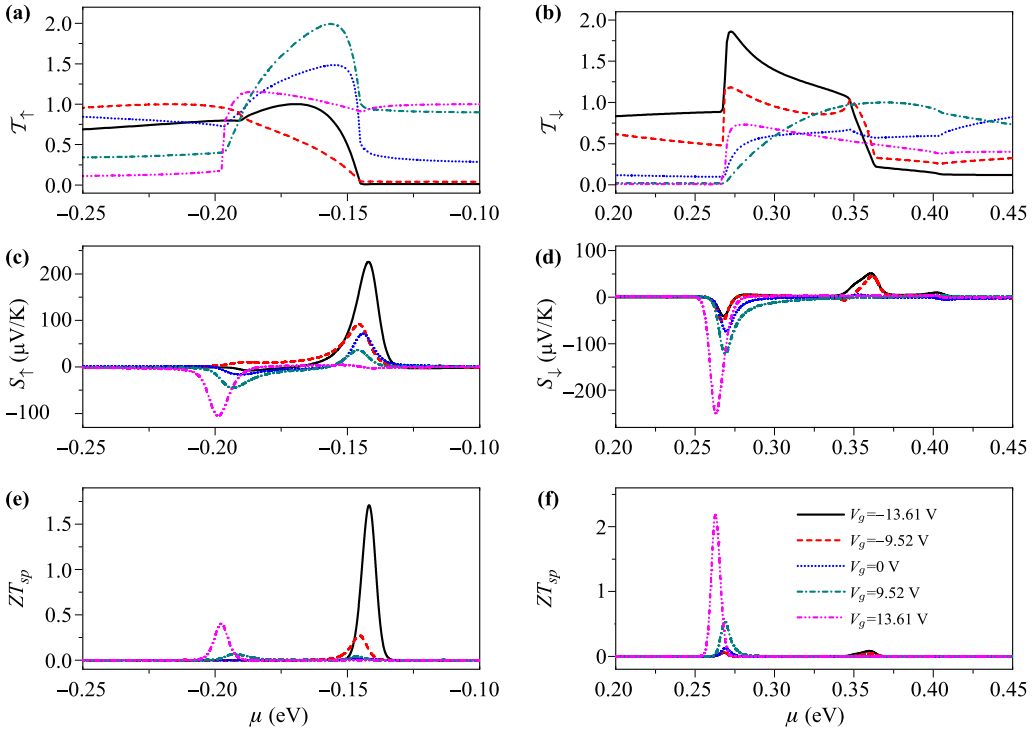

Fig. 8 **(a)** $\mathcal{T}_\uparrow$, **(b)** $\mathcal{T}_\downarrow$, **(c)** $S_\uparrow$, **(d)** $S_\downarrow$, and **(e, f)** ZT_{sp} versus chemical potential for the FM configuration of the molecular junction with $N = 6$ under different gate voltage. All the curves in the panels from (c) to (f) are obtained at $T = 20$ K.

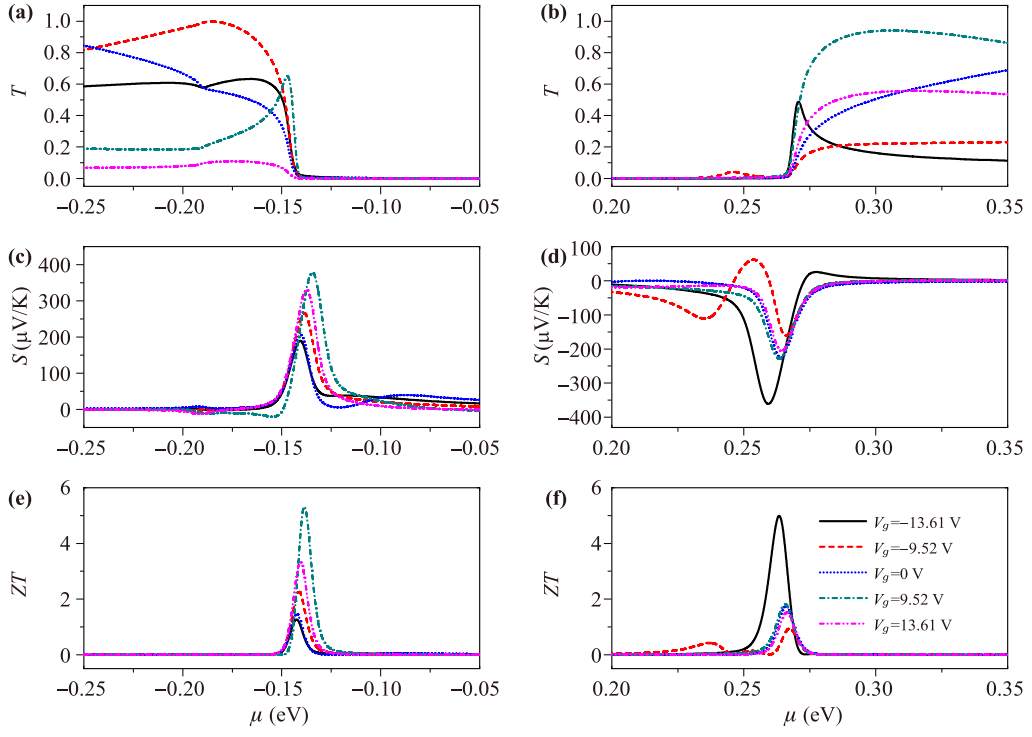

Fig. 9 **(a, b)** T, **(c, d)** S, and **(e, f)** ZT versus chemical potential for AFM configuration of the molecular junction with $N = 6$ under different gate voltage. All the curves in the panels from (c) to (f) are obtained at $T = 20$ K.

Figs. 9(e) and (f). The figure of merit near the left and right transmission gaps can reach ∼5 at specific gate voltages. The large value of the figure of merit implies that ZGNR-polyacene-ZGNR junctions are outstanding thermoelectric devices in the AFM configuration.

4 Summary

In summary, we have investigated spin-resolved electronic and thermoelectric transport in a series of graphene-based nanojunctions by using first-principles calculation. Numerical results show that spin-resolved conductance increases versus junction length in FM configurations and its magnitude can be adjusted by the gate voltage with ∼3.6% gating efficiency. Owing to the very small conductance of the AFM configurations, very large TMR from 10^4 to 10^5 can be achieved for the nanojunctions. The system is changed from capacitive-like to inductive-like with increasing junction length in the FM configuration, whereas the system always exhibits capacitive-like behavior in the AFM configuration. The spin-up thermopower and spin-down thermopower are of opposite sign, which indicates opposite flowing directions of heat-induced spin-resolved currents. More importantly, thermally induced pure spin-resolved current and pure spin current can be obtained by adjusting the gate voltage. Large figures of merit can be achieved by adjusting the chemical potential and the gate voltage. Numerical results indicate that ZGNR-polyacene-ZGNR nanojunctions are good candidates for spintronic and thermoelectronic devices.

Acknowledgements This work was financially supported by grant from the National Natural Science Foundation of China (Grant Nos. 11304205 and 11404273) and Shenzhen Natural Science Foundation (No. JCYJ20130326111836781).

References

1. A. Aviram and M. A. Ratner, Molecular rectifiers, *Chem. Phys. Lett.* 29(2), 277 (1974)
2. C. Dekker, S. J. Tans, and A. R. M. Verschueren, Room temperature transistor based on a single carbon nanotube, *Nature* 393(6680), 49 (1998)
3. B. Q. Xu and N. J. Tao, Measurements of single-molecule electromechanical properties, *Science* 301(5637), 1121 (2003)
4. S. V. Aradhya and L. Venkataraman, Single-molecule junctions beyond electronic transport, *Nat. Nanotechnol.* 8(6), 399 (2013)
5. W. X. Lai, C. Zhang, and Z. S. Ma, Single molecular shuttle junction: Shot noise and decoherence, *Front. Phys.* 10(1), 108501 (2015)
6. Z. Y. Ning, J. S. Qiao, W. Ji, and H. Guo, Correlation of interfacial bonding mechanism and equilibrium conductance of molecular junctions, *Front. Phys.* 9(6), 780 (2014)
7. W. Zhu, A. M. Guo, and Q. F. Sun, Electronic transport through tetrahedron-structured DNA-like system, *Front. Phys.* 9(6), 774 (2014)
8. W. Ji, H. Q. Xu, and H. Guo, Quantum description of transport phenomena: Recent progress, *Front. Phys.* 9(6), 671 (2014)
9. K. S. Novoselov, V. I. Fal′ko, L. Colombo, P. R. Gellert, M. G. Schwab, and K. Kim, A roadmap for graphene., *Nature* 490(7419), 192 (2012)
10. M. C. Lemme, D. C. Bell, J. R. Williams, L. A. Stern, B. W. H. Baugher, P. Jarillo-Herrero, and C. M. Marcus, Etching of graphene devices with a helium ion beam, *ACS Nano* 3(9), 2674 (2009)
11. L. C. Campos, V. R. Manfrinato, J. D. Sanchez-Yamagishi, J. Kong, and P. Jarillo-Herrero, Anisotropic etching and nanoribbon formation in single-layer graphene, *Nano Lett.* 9(7), 2600 (2009)
12. P. Avouris, Z. H. Chen, and V. Perebeinos, Carbon-based electronics, *Nat. Nanotechnol.* 2(10), 605 (2007)
13. L. Britnell, R. V. Gorbachev, R. Jalil, B. D. Belle, F. Schedin, A. Mishchenko, T. Georgiou, M. I. Katsnelson, L. Eaves, S. V. Morozov, N. M. R. Peres, J. Leist, A. K. Geim, K. S. Novoselov, and L. A. Ponomarenko, Field-effect tunneling transistor based on vertical graphene heterostructures, *Science* 335(6071), 947 (2012)
14. Z. H. Qiao, J. Jung, Q. Niu, and A. H. MacDonald, Electronic highways in bilayer graphene, *Nano Lett.* 11(8), 3453 (2011)
15. X. F. Li and Y. Luo, Conductivity of carbon-based molecular junctions from *ab-initio* methods, *Front. Phys.* 9(6), 748 (2014)
16. B. Wang, J. Wang, and H. Guo, Ab initio calculation of transverse spin current in graphene nanostructures, *Phys. Rev. B* 79(16), 165417 (2009)
17. B. Wang, R. Chu, J. Wang, and H. Guo, First-principles calculation of chiral current and quantum self-inductance of carbon nanotubes, *Phys. Rev. B* 80(23), 235430 (2009)
18. B. Wang, and J. Wang, First-principles investigation of transport properties through longitudinal unzipped carbon nanotubes, *Phys. Rev. B* 81(4), 045425 (2010)
19. J. Wang, Time-dependent quantum transport theory from non-equilibrium Green's function approach, *J. Comput. Electron.* 12(3), 343 (2013)
20. Y. H. Kwok, Y. Zhang, and G. H. Chen, Time-dependent density functional theory for quantum transport, *Front. Phys.* 9(6), 698 (2014)
21. L. Liao, Y. C. Lin, M. Q. Bao, R. Cheng, J. W. Bai, Y. A. Liu, Y. Q. Qu, K. L. Wang, Y. Huang, and X. F. Duan, High-speed graphene transistors with a self-aligned nanowire gate, *Nature* 467(7313), 305 (2010)

22. Y. M. Lin, A. Valdes-Garcia, S. J. Han, D. B. Farmer, I. Meric, Y. N. Sun, Y. Q. Wu, C. Dimitrakopoulos, A. Grill, P. Avouris, and K. A. Jenkins, Wafer-Scale Graphene Integrated Circuit, *Science* 332(6035), 1294 (2011)
23. C. Sire, F. Ardiaca, S. Lepilliet, J.W. T. Seo, M. C. Hersam, G. Dambrine, H. Happy, and V. Derycke, Flexible gigahertz transistors derived from solution-based single-layer graphene, *Nano Lett.* 12(3), 1184 (2012)
24. N. Petrone, I. Meric, J. Hone, and K. L. Shepard, Graphene field-effect transistors with gigahertz-frequency power gain on flexible substrates, *Nano Lett.* 13(1), 121 (2013)
25. J. Maciejko, J. Wang, and H. Guo, Time-dependent quantum transport far from equilibrium: An exact nonlinear response theory, *Phys. Rev. B* 74(8), 085324 (2006)
26. B. Wang, Y. Xing, L. Zhang, and J. Wang, Transient dynamics of molecular devices under a steplike pulse bias, *Phys. Rev. B* 81(12), 121103(R) (2010)
27. Y. X. Xing, B. Wang, and J. Wang, First-principles investigation of dynamical properties of molecular devices under a steplike pulse, *Phys. Rev. B* 82(20), 205112 (2010)
28. L. Zhang, Y. X. Xing, and J. Wang, First-principles investigation of transient dynamics of molecular devices, *Phys. Rev. B* 86(15), 155438 (2012)
29. L. Zhang, J. Chen, and J. Wang, First-principles investigation of transient current in molecular devices by using complex absorbing potentials, *Phys. Rev. B* 87(20), 205401 (2013)
30. B. G. Wang, J. Wang, and H. Guo, Current partition: A nonequilibrium Green's function approach, *Phys. Rev. Lett.* 82(2), 398 (1999)
31. M. Büttiker, A. Prêtre, and H. Thomas, Dynamic conductance and the scattering matrix of small conductors, *Phys. Rev. Lett*, 1993, 70(26): 4114; M. Buttiker, Dynamic conductance and quantum noise in mesoscopic conductors, *J. Math. Phys.* 37(10), 4793 (1996)
32. D. Kienle, M. Vaidyanathan, and F. Léonard, Self-consistent AC quantum transport using nonequilibrium Green functions, *Phys. Rev. B* 81(11), 115455 (2010)
33. Y. D. Wei and J. Wang, Current conserving nonequilibrium AC transport theory, *Phys. Rev. B* 79(19), 195315 (2009)
34. Y. J. Yu, H. X. Zhan, Y. D. Wei, and J. Wang, Current-conserving and gauge-invariant quantum AC transport theory in the presence of phonon, *Phys. Rev. B* 90(7), 075407 (2014)
35. Y. J. Yu, B. Wang, and Y. D. Wei, AC response of a carbon chain under a finite frequency bias, *J. Chem. Phys.* 127(10), 104701 (2007)
36. B. Wang and J. Wang, Charge relaxation resistance at atomic scale: An *ab initio* calculation, *Phys. Rev. B* 77(24), 245309 (2008)
37. B. Wang, Y. J. Yu, L. Zhang, Y. D. Wei, and J. Wang, Oscillation of dynamic conductance of Al-C n-Al structures: Nonequilibrium Green's function and density functional theory study, *Phys. Rev. B* 79(15), 155117 (2009)
38. L. Zhang, B. Wang, and J. Wang, First-principles investigation of alternating current density distribution in molecular devices, *Phys. Rev. B* 86(16), 165431 (2012)
39. H. Zhang, K. S. Chan, and Z. J. Lin, The dynamical conductance of graphene tunnelling structures, *Nanotechnology* 22(50), 505705 (2011)
40. C. Roland, M. B. Nardelli, J. Wang, and H. Guo, Dynamic conductance of carbon nanotubes, *Phys. Rev. Lett.* 84(13), 2921 (2000)
41. Z. Z. Yu and J. Wang, Transport properties of WSe2 nanotube heterojunctions: A first-principles study, *Phys. Rev. B* 91(20), 205431 (2015)
42. D. G. Cahill, W. K. Ford, K. E. Goodson, G. D. Mahan, A. Majumdar, H. J. Maris, R. Merlin, and S. R. Phillpot, Nanoscale thermal transport, *J. Appl. Phys.* 93(2), 793 (2003)
43. J. P. Bergfield and C. A. Stafford, Thermoelectric signatures of coherent transport in single-molecule heterojunctions, *Nano Lett.* 9(8), 3072 (2009)
44. X. T. Jia and K. Xia, Electric and thermo spin transfer torques in Fe/Vacuum/Fe tunnel junction, *Front. Phys.* 9(6), 768 (2014)
45. K. Uchida, S. Takahashi, K. Harii, J. Ieda, W. Koshibae, K. Ando, S. Maekawa, and E. Saitoh, Observation of the spin Seebeck effect, *Nature* 455(7214), 778 (2008)
46. K. Uchida, J. Xiao, H. Adachi, J. Ohe, S. Takahashi, J. Ieda, T. Ota, Y. Kajiwara, H. Umezawa, H. Kawai, G. E. W. Bauer, S. Maekawa, and E. Saitoh, Spin Seebeck insulator, *Nat. Mater.* 9(11), 894 (2010)
47. H. Adachi, K. Uchida, E. Saitoh, and S. Maekawa, Theory of the spin Seebeck effect, *Rep. Prog. Phys.* 76(3), 036501 (2013)
48. J. S. Wang, B. K. Agarwalla, H. Li, and J. Thingna, Nonequilibrium Green's function method for quantum thermal transport, *Front. Phys.* 9(6), 673 (2014)
49. B. Z. Rameshti and A. G. Moghaddam, Spin-dependent Seebeck effect and spin caloritronics in magnetic graphene, *Phys. Rev. B* 91(15), 155407 (2015)
50. J. W. Li, B. Wang, F. M. Xu, Y. D. Wei, and J. Wang, Spin-dependent Seebeck effects in graphene-based molecular junctions, *Phys. Rev. B* 93(19), 195426 (2016)
51. Y. M. Zuev, W. Chang, and P. Kim, Thermoelectric and magnetothermoelectric transport measurements of graphene, *Phys. Rev. Lett.* 102(9), 096807 (2009)
52. M. G. Zeng, Y. P. Feng, and G. C. Liang, Graphene-based Spin Caloritronics, *Nano Lett.* 11(3), 1369 (2011)
53. Z. Y. Zhao, X. C. Zhai, and G. J. Jin, Bipolar-unipolar transition in thermospin transport through a graphene-based transistor, *Appl. Phys. Lett.* 101(8), 083117 (2012)

54. J. Taylor, H. Guo, and J. Wang, Ab initio modeling of open systems: Charge transfer, electron conduction, and molecular switching of a C_{60} device, *Phys. Rev. B* 63(12), 121104 (2001)

55. D. R. Hamann, M. Schluter, and C. Chiang, Norm-Conserving Pseudopotentials, *Phys. Rev. Lett.* 43(20), 1494 (1979)

56. O. Gunnarsson and B. I. Lundqvist, Exchange and correlation in atoms, molecules, and solids by the spin-density functional formalism, *Phys. Rev. B* 13(10), 4274 (1996)

57. M. Büttiker, Y. Imry, R. Landauer, and S. Pinhas, Generalized many-channel conductance formula with application to small rings, *Phys. Rev. B* 31(10), 6207 (1985)

58. T. Rejec, A. Ramsak, and J. H. Jefferson, Spin-dependent thermoelectric transport coefficients in near perfect quantum wires, *Phys. Rev. B* 65(23), 235301 (2002)

59. B. Wang, J. W. Li, Y. J. Yu, Y. D. Wei, J. Wang, and H. Guo, Giant tunnel magneto-resistance in graphene based molecular tunneling junction, *Nanoscale* 8(6), 3432 (2016)

60. J. Nakabayashi, D. Yamamoto, and S. Kurihara, Band selective filter in a zigzag graphene nanoribbon, *Phys. Rev. Lett.* 102(6), 066803 (2009)